ACES Asian Chemical Editorial Society

DOI: 10.1002/asia.202000131

CHEMISTRY AN ASIAN JOURNAL Full Paper

VIP

Preparations, Structures and Luminescence Properties of Penta-rare-earth Incorporated Tetravacant Dawson Selenotungstates and Their Ho^{3+}/Tm^{3+} Co-doped Derivatives

Yan Zhang, Yi-Fan Liu, Xin Xu, Li-Juan Chen,* and Jun-Wei Zhao*[a]

Abstract: A family of penta-rare-earth incorporated tetravacant Dawson selenotungstates $[H_2N(CH_3)_2]_{10}H_3[SeO_4RE_5(H_2O)_7(Se_2W_{14}O_{52})_2]\cdot 40H_2O$ [RE = Ho^{3+} (**1**), Er^{3+} (**2**), Tm^{3+} (**3**), Tb^{3+} (**4**)] were synthesized. It should be noted that a penta-RE $[SeO_4RE_5(H_2O)_7]^{11+}$ central core connecting two tetra-vacant Dawson-type $[Se_2W_{14}O_{52}]^{12-}$ subunits generates a dimeric assembly of $[SeO_4RE_5(H_2O)_7(Se_2W_{14}O_{52})_2]^{13-}$ in the structures of **1**–**4**. Meanwhile, a class of Ho^{3+}/Tm^{3+} co-doped derivatives based on **1** with a Ho^{3+}/Tm^{3+} molar ratio of 0.75:0.25–0.25:0.75 were also prepared and characterized by energy-dispersive spectroscopy (EDS) analyses. Moreover, their luminescence properties were systematically investigated, which indicate that Tm^{3+} ions can sensitize the emission of Ho^{3+} ions in the visible region and prolong the fluorescence lifetime of Ho^{3+} ions to some extent. Energy transfer from Tm^{3+} ions to Ho^{3+} ions was probed by time-resolved emission spectroscopy (TRES), and the CIE 1931 diagram has been applied to evaluate all possible luminescence colors.

Introduction

Polyoxometalates (POMs) are a kind of polynuclear metal-oxo clusters comprising of early transition metals and oxygen atoms and have attracted enormous concern for their diverse structures and potential applications in catalysis, magnetism, materials science, medicine, proton conductivity and so on.[1] Among them, to date, a large number of transition-metal (TM) or/and rare-earth (RE) containing polyoxotungstate (POT) derivatives with beauteous structures and interesting have been successively synthesized.[2] Selenotungstates (STs) as a significant branch of POTs have appealed to increasing research enthusiasm in the past several years. As far as we know, the one-pot self-assembly strategy has been always used to prepare ST derivatives on account of the lack of ST precursors.[3] The stereochemical lone electron pair active SeO_3^{2-} ion is often utilized as a starting material to react with tungstates to construct the open-skeleton ST building blocks, which provides an excellent opportunity for constructing diversified TM or RE incorporated ST derivatives.[4]

Under these considerations, some unprecedented and intriguing STs have been triumphantly synthesized under precise control of one-pot reaction conditions.[5] For example, in 2006, Niu's group discovered a copper-complex decorated saturated Keggin-type ST $[Cu_2(2,2'\text{-bpy})_4Cl][Cu(2,2'\text{-bpy})_2\text{-}SeW_{12}O_{40}]\cdot 2H_2O$ (2,2′-bpy = 2,2′-bipyridine).[5a] In 2013, Cronin and his collaborators obtained a series of unexpected gigantic nanomolecular clusters from dimeric $[H_{10}Se_2W_{29}O_{103}]^{14-}$ to dodecameric $[H_{18}Cu_9Cl_3(H_2O)_{18}(Se_2W_{29}O_{102})_6]^{99-}$ by introducing different TM ions and flexible pH control via the one-pot synthetic strategy.[5b] In 2014–2016, Su et al. reported a multi-Fe^{III}-substituted tetrameric ST $[Fe_{10}Se_8W_{62}O_{222}(OH)_{18}(H_2O)_4]^{28-}$ derived from $[H_{10}Se_2W_{29}O_{103}]^{14-}$ building block,[5c] and a Mn-containing dimeric ST $[K_2\subset\{MnSe_4W_{23}O_{85}(H_2O)_6\}]^{12-}$ consisting of two unreported Dawson-type $\{Se_2W_{11}\}$ fragments.[5d] Through extensive literature research, it can be apparently found that the majority of studies are concentrated on TM-containing STs, however, examples of RE containing STs (RECSTs) have been rarely addressed.[6]

On one hand, RE ions generally have the high coordination numbers, flexible coordination modes and strong oxophilicity and can behave as powerful capabilities to connect ST fragments into large aggregates.[6a–b] For instance, in 2013, Su and his co-workers firstly isolated two gigantic $\{W_4\}$-bridging octameric RECSTs $[\{(SeO_3)W_{10}O_{34}\}_8\{Ce_8(H_2O)_{20}\}(WO_2)_4(W_4O_{12})]^{48-}$ and $[\{(SeO_3)W_{10}O_{34}\}_8\{Ce_8(H_2O)_{20}\}(WO_2)_4\{(W_4O_6)Ce_4(H_2O)_{14}\text{-}(SeO_3)_4(NO_3)_2\}]^{34-}$.[5e] Subsequently, they reported a trimeric Keggin-type Ce-containing ST $[(\alpha\text{-}SeW_9O_{33})_2(Ce_2(H_2O)_4W_3O_6)\{\alpha\text{-}Se_2W_{14}O_{51}(OH)\}]^{15-}$ polyanion, which is assembled from two trilacunary $[\alpha\text{-}SeW_9O_{33}]^{8-}$ units and a tetra-vacant Dawson-type $[\alpha\text{-}Se_2W_{14}O_{51}(OH)]^{11-}$ unit encapsulating a $[Ce_2(H_2O)_4W_3O_6]^{12+}$ cluster.[6c] In 2019, our group prepared di-Ce^{3+}-substituted hexameric ST $[Ce_2W_4O_9(H_2O)_7(SeW_9O_{33})_3]_2^{24-}$.[6d] However, the research on RECSTs is still in the infancy, especially for the high-nuclearity RECSTs.[7] On the other hand, the incorporation of RE centers to POM matrixes can endow POM-based materials with interesting luminescence performances for applications in white light-emitting diodes, electroluminescent materials, bio-sensing technologies and so on,[8] because RE ions own abundant 4f energy levels so that they can give out characteristic emissions and long decay lifetimes in the ultraviolet, visible and near-

[a] Dr. Y. Zhang, Y.-F. Liu, X. Xu, Prof. L.-J. Chen, Prof. Dr. J.-W. Zhao
Henan Key Laboratory of Polyoxometalate Chemistry
College of Chemistry and Chemical Engineering
Henan University
Kaifeng 475004 (China)
E-mail: ljchen@henu.edu.cn
zhaojunwei@henu.edu.cn

Supporting information for this article is available on the WWW under https://doi.org/10.1002/asia.202000131

infared ranges via f-f transitions. As a result, it is vey imperative to design the available strategy for preparing novel high-nuclearity RECSTs.

Noteworthily, some researches have been concentrated on the photoluminescence properties of homo-RE incorporated POTs in the past two decades whereas research results demonstrate that homo-RE incorporated POTs can't meet the requirement of light emitting materials because of some limitations such as high color drift, low luminescence intensity and low photostability.[9] To resolve these problems, recently, hetero-RE co-doped POT-based materials have become a research hotspot. For instance, a series of Dy^{3+}/Er^{3+} co-doped POT materials were employed to enhance luminous stability of Dy^{3+} ions,[10a] and Yb^{3+}/Er^{3+} co-doped tellurotungstates were used to enhance luminescence intensity through up-conversion luminescence.[10b] Nonetheless, examples for probing energy transfer between RE ions in hetero-RE co-doped POTs are still rarely known. Therein, trivalent Tm^{3+} ions can provide a blue emission light through f-f $^1D_2 \rightarrow {}^3F_4$ transition, which can perfectly overlap with the $^5I_8 \rightarrow {}^5G_6$ excitation transition of Ho^{3+} ions further emitting red emission caused by $^5F_5 \rightarrow {}^5I_8$ transition.[10c] Therefore the overlap between emission peak of Tm^{3+} and excitation peak of Ho^{3+} ions provide favorable support for energy transfer exploration, and the molar concentration ratio of Ho^{3+}/Tm^{3+} can be controlled to tune the emission color in Ho^{3+}/Tm^{3+} co-doped POT system.

In this work, following the one-pot self-assembly method, four tetra-vacant penta-RE incorporated Dawson-type STs $[H_2N(CH_3)_2]_{10}H_3[SeO_4RE_5(H_2O)_7(Se_2W_{14}O_{52})_2]\cdot 40H_2O$ [RE = Ho^{3+} (**1**), Er^{3+} (**2**), Tm^{3+} (**3**), Tb (**4**)] were synthesized successfully by reaction of the mixture of $RE(NO_3)_3\cdot 6H_2O$, Na_2SeO_3, $Na_2WO_4\cdot 2H_2O$ and dimethylamine hydrochloride (DMA·HCl) in acid aqueous solution. Herein, some Se^{IV} atoms not only function as central heteroatoms in tetra-vacant Dawson-type ST fragments, but also some Se^{IV} atoms exhibit a tetragonal pyramid coordination geometry surrounded by five RE ions so that they play a vital anionic templating role in the structures. Besides, DMA·HCl can be treated as an organic solubilizer to improve the reactivity of tungstates and RE ions, simultaneously, it can effectively reduce precipitation led by the rapid combination of tungstates and RE ions. The photoluminescence (PL) emission, excitation spectra, decay lifetime curves, time-resolved emission spectra (TRES) and CIE 1931 diagram are employed to characterize the luminescence properties of **1**–**4**. Furthermore, we have first synthesized a series of Ho^{3+}/Tm^{3+} co-doped STs $[H_2N(CH_3)_2]_{10}H_3[SeO_4RE_5(H_2O)_7(Se_2W_{14}O_{52})_2]\cdot 40H_2O$ (RE = **$Ho_{0.75}/Tm_{0.25}$**, **$Ho_{0.67}/Tm_{0.33}$**, **$Ho_{0.5}/Tm_{0.5}$**, **$Ho_{0.33}/Tm_{0.67}$**, **$Ho_{0.25}/Tm_{0.75}$**) to investigate the energy transfer mechanism between Ho^{3+} and Tm^{3+} ions and emission color-tunable property. This work provides us enlightening ideas to develop novel hetero-RE co-doped POM materials and lays an important foundation for functional exploitation. In addition, the research on luminescence study for Ho^{3+}/Tm^{3+} co-doped STs not only contributes to broaden the applications of RE–POM functional materials in the field of solid- state lighting materials, but also can exhibit great potentials of white light-emitting aspects.

Results and Discussion

Structural description

The PXRD spectra of **1**–**4** are well consistent with the simulative XRD spectra from single-crystal structure analysis, indicating that all the samples are pure (Figure S1 in the Supporting Information). **1**–**4** are isomorphic and crystallize in the monoclinic space group *C*2/m, so only **1** is described as a representative in detail. The molecular structure of **1** is composed of a dimeric sandwich-type polyanion $[SeO_4Ho_5(H_2O)_7(Se_2W_{14}O_{52})_2]^{13-}$ (**1 a**), ten $[H_2N(CH_3)_2]^+$ ions, three protons, and forty lattice water molecules. Thereinto, protonated dimethylamine species serving as counter cations can promote the stability of the whole structure, which is an important factor in the process of the resulting products.[11] The dimeric **1 a** polyanion (Figure 1a) consists of two tetra-vacant Dawson-type $[Se_2W_{14}O_{52}]^{12-}$ units capturing a $[SeO_4Ho_5(H_2O)_7]^{11+}$ cluster through lacunary oxygen atoms from $[Se_2W_{14}O_{52}]^{12-}$ fragments (Figure 1b). The SeO_3^{2-} heteroanion template plays a significant role in the formation of the lacunary polyoxoanion structure, owing to the inducing effect of the lone pair of electrons on the SeO_3^{2-} anion. The $[Se_2W_{14}O_{52}]^{12-}$ units (Figure 1c) have considerable tendency to embed more metal centers through lacunary binding sites. In the basic tetra-lacunary $[Se_2W_{14}O_{52}]^{12-}$ units, all the W atoms are located in the centers of octahedra with W–O distances of 1.716(10)–2.480(9) Å and O–W–O band angles of 69.1(4)–173.7(5)°. All the Se heteroatoms show the triangular pyramidal coordination configuration with Se–O distances of 1.687(9)–1.749(8) Å and the O–Se–O angles of 99.2(4)–102.0(4)°. Furthermore, the $[SeO_4Ho_5(H_2O)_7]^{11+}$ fragment is described in Figure 1d. Five Ho^{3+} linkers and a disordered {SeO_4} segment constitute the $[SeO_4Ho_5(H_2O)_7]^{11+}$ subunit during the self-assembly. The crystallographically unique $Ho1^{3+}$ cation binds to two μ_3-O atoms (O15, O15A), two μ_2-O atoms (O5, O5A) from $[Se_2W_{14}O_{52}]^{12-}$ building blocks [Ho–O: 2.300(11)–2.335(9) Å], two coordinated water O atoms (O1W, O2W) [Ho–O: 2.30(3)–2.83(4) Å] and another two O atoms O27, O28B from a {$SeO_4Ho_5(H_2O)_7$} cluster [Ho–O: 2.34(3)–2.275(14) Å], achieving an eight-coordinate bicapped trigonal-prismatic geometry, in which two triangle planes are occupied by the O1W, O15, O5 group and the O5A, O27, O28B group, respectively, and two cap positions are taken up by O15A and O2W (Figure 1e). Besides, the crystallographically independent $Ho2^{3+}$ cation exhibits the similar coordination geometry. Under careful observation, the bicapped trigonal-prismatic geometry of the $Ho2^{3+}$ ion is constructed from two μ_2-O atoms (O13, O13A), two μ_3-O atoms (O19, O19A) of lacunary $[Se_2W_{14}O_{52}]^{12-}$ fragments [Ho–O: 2.307(9)–2.378(9) Å], two coordinated water O atoms (O2WB, O3W) [Ho–O: 2.34(2)–2.55(3) Å] and O27, O28B atoms inhabit in a {$SeO_4Ho_5(H_2O)_7$} mental ring [Ho–O: 2.41(3)–2.330(14) Å] (Figure 1f). Besides, O3W, O19A and O13A atoms sit on the vertexes of the triangle plane, O13, O27A, O28 group are located on vertexes of another triangle plane in the bicapped trigonal-prismatic geometry, meanwhile O19 and O2WB atoms root in two cap positions. And Ho1, Ho2, Ho1B and Ho2B graft each

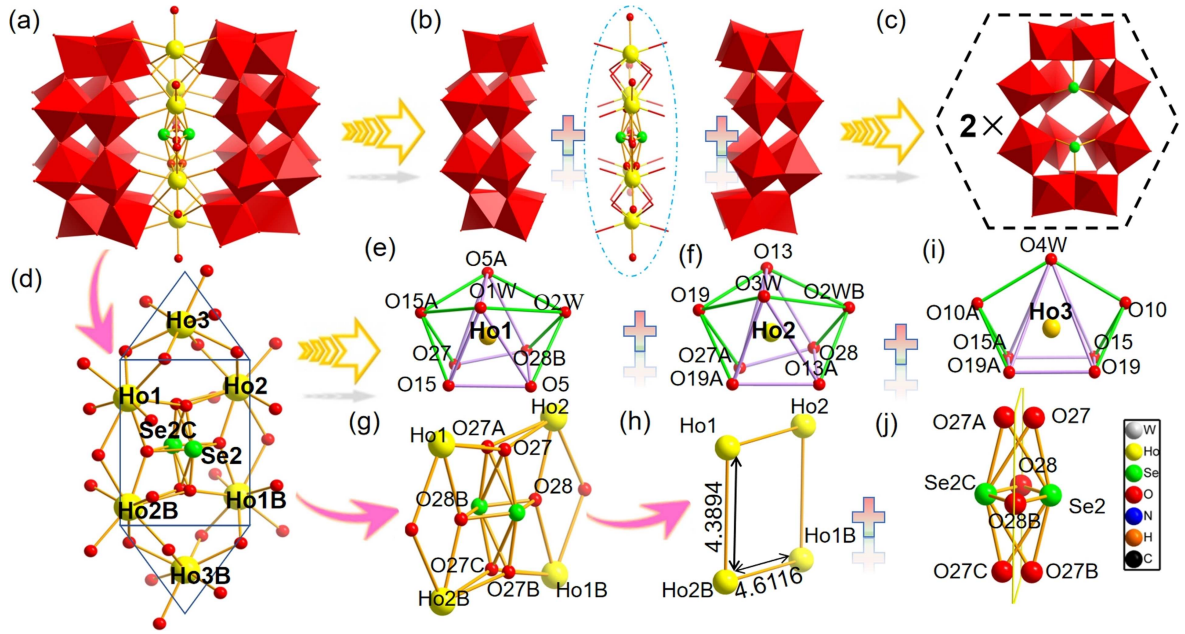

Figure 1. a) The presentation of **1 a**; b) Schematic breakdown drawing of **1 a**; c) The tetra-vacant Dawson-type $[Se_2W_{14}O_{52}]^{12-}$ in **1**; d) View of the $[SeO_4Ho_5(H_2O)_7]^{11+}$ cluster; e–f) The coordination geometry of the $Ho1^{3+}$ and $Ho2^{3+}$ ions; g) View of the $[SeO_4Ho_4(H_2O)_6]^{8+}$ group; h) The alignment of four Ho^{3+} ions in $[SeO_4Ho_4(H_2O)_6]^{8+}$; i) The coordination geometry of the $Ho3^{3+}$ ion and j) The combination mode of O28 and disordered O27 and Se2 atoms. (A: x, -y, z, B: 1-x, y, -z, C: 1-x, -y, -z, (W: gray; Ho: yellow; Se: green; O: red; N: dark blue; H: orange-yellow; C: black).

other via O bridges to construct a $\{Ho_4\}$ square in the center of the POM skeleton. Four Ho^{3+} ions are situated on four vertexes of the $\{Ho_4\}$ cluster in the $[SeO_4Ho_5(H_2O)_7]^{11+}$ fragment (Figure 1g–h) with two neighboring edges of 4.3894 and 4.6116 Å, which is quite similar to another four Dy^{3+} ions in $[Dy_4W_8O_{19}(H_2O)_{10}(OH)_2(Ser)_2]^{20+}$ (Ser = serine) reported before (Figure S2 in the supporting information).[11] Compared with $[SeO_4Ho_5(H_2O)_7]^{11+}$ cluster, the mental ring in $[Dy_4W_8O_{19}(H_2O)_{10}(OH)_2(Ser)_2]^{20+}$ cluster simultaneously consists of RE and W atoms. In addition, it's worth noting that the disordered $Ho3^{3+}$ ion is distributed at two sites (Ho3 Ho3B) of the $\{Ho_4\}$ cluster with 50% site occupancy (Figure 1d). And the $Ho3^{3+}$ ion establishes a distorted bicapped square-pyramidal geometry, which is defined by six O atoms (O10, O10A, O15, O15A, O19 and O19A) of vacant sites of two $[Se_2W_{14}O_{52}]^{12-}$ fragments [Ho–O: 2.389(10)–2.533(10) Å], a coordinated water atom O4W [Ho–O: 2.44(4) Å]. Moreover, O15, O15A, O19 and O19A atoms make up the bottom plane of the bicapped square-pyramidal, O4W atom is located on the vertex position, and bridging O10 and O10A atoms sit on the capped sites (Figure 1i). Besides, the distorted Se2 atom is encapsulated in the cavity of $\{Ho_4\}$ segment and contributes to stability of the centrosymmetric $\{SeO_4Ho_5(H_2O)_7\}$ cluster, which is infrequent among the POM architectures (Figure 1j).

Furthermore, the 3-D stacking mode of **1 a** is illustrated in detail in Figure 2a. To decrease steric hindrance,[12] dimeric **1 a** polyanions are regularly arranged in the staggered fashion, demonstrating a -ABAB- pattern between adjacent layers viewed along *a* axis (Figure 2b). dimeric **1 a** polyanions are regularly organized in -AAA- fashion in the layer A or layer B (Figure 2c–f). Analogously, dimeric **1 a** polyanions are distributed in the model of -AAA- in the view of *ab* or *ac* plane (Figure S3a–d in the supporting information). It is easily observed that dimeric **1 a** polyanions interact with monoprotonated by $[H_2N(CH_3)_2]^+$ cations by means of hydrogen bonding interactions between N atoms rooting in $[H_2N(CH_3)_2]^+$ and O atoms from dimeric **1 a** polyanions with the N–H•••O distances ranging from 2.94(2) to 3.22(2) Å (Figure 2g–h).

Photoluminescence (PL) properties

In recent years, RE-based materials have appealed great interest and been widely used in various fields because RE elements own special electronic configurations and abundant energy levels, which endow them a number of advantages, such as high conversion efficiency, high color purity and abundant luminescent color.[13] On account of the intra 4f–4f transitions, each RE ion has its characteristic emission peaks. Thus, various wavelengths of light from the ultraviolet to infrared region can be absorbed or emitted by RE ions to form a variety of luminous materials. Hence, PL properties and lifetime decay behaviors of solid-state **1**–**3** were studied at room temperature. With aim of decreasing the influence of other factors on fluorescence signals, 0.5 g pure materials are pressed into pieces (Figure S4 in the supporting information). When **1** was excited by an ultraviolet light of 454 nm, two characteristic emission bands at 575 and 664 nm (Figure 3a) appear in the emission spectrum from 520 to 750 nm, which are assigned to Ho^{3+} $^5F_4 + {}^5S_2 \rightarrow {}^5I_8$ and $^5F_5 \rightarrow {}^5I_8$ transitions.[14a–b] Meanwhile, by monitoring the emission at 664 nm, its excitation spectrum with three characteristic excitation peaks at 418, 454 and 486 nm were gathered,

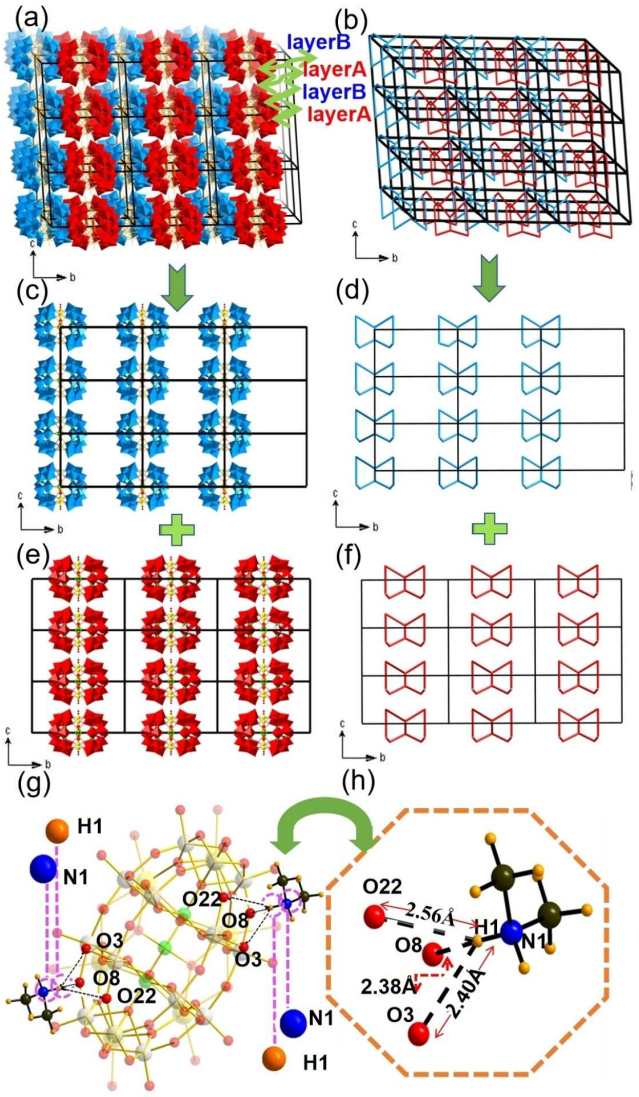

Figure 2. a) The supramolecular 3-D stacking of **1 a**; b) The simplified 3-D stacking of **1 a**; c) View of layer B; d) The simplified view of layer B; e) View of layer A; f) The simplified view of layer A; g) Hydrogen-bonding interactions between N atoms on $[H_2N(CH_3)_2]^+$ cations and surface O atoms of polyanions and h) The distances between donor N1 atom and acceptor O atoms.

and three peaks correspond to $^5I_8 \rightarrow {}^5G_5$, $^5I_8 \rightarrow {}^5G_6$ and $^5I_8 \rightarrow {}^5F_3$ transitions of Ho^{3+} ions, respectively (Figure 3b). To further understand the fluorescence lifetime of **1**, the decay time curve was gained based on monitoring the main emission peak at 664 nm.[14c–d] The decay time curve of **1** was matched with a second-order exponential function $I = A_1\exp(t/\tau_1) + A_2\exp(t/\tau_2)$ (Figure 3c). τ_1 is 0.87 μs (55.78%), τ_2 is 7.80 μs (44.22%) and A_1 and A_2 are 2987.35 and 264.59. Through the equation $\tau^* = (A_1\tau_1^2 + A_2\tau_2^2)/(A_1\tau_1 + A_2\tau_2)$, the average lifetime ($\tau^*$) of **1** can be calculated as $\tau^* = 4.08$ μs (Table S1a in the supporting information).[15] When **2** was excited under an ultraviolet light of 381 nm, the emission spectrum of **2** in 525–725 nm was acquired and presents three characteristic emissions at 538, 556 and 700 nm, which are attributed to Er^{3+} $^2I_{11/2} \rightarrow {}^4I_{15/2}$, $^2S_{3/2} \rightarrow {}^4I_{15/2}$, $^4F_{9/2} \rightarrow {}^4I_{15/2}$ transitions, respectively (Figure 3d).[16] By supervising the strongest $^4S_{3/2} \rightarrow {}^4I_{15/2}$ emission of the Er^{3+} ion at 556 nm, the excitation spectrum of **2** was obtained and displays three groups of excitation bands at 372, 401, and 424 nm, which are assigned to the $^4I_{15/2} \rightarrow {}^2H_{9/2}$, $^4G_{11/2} \rightarrow {}^4I_{15/2}$ and $^4I_{15/2} \rightarrow {}^4H_{9/2}$ transitions of the Er^{3+} ion, respectively (Figure 3e).[17] The luminescent decay curve was measured by supervising the main emission at 556 nm and the result was in good agreement with a second-order exponential function. τ_1 is 0.86 μs (42.46%), τ_2 is 7.50 μs (57.54%) and A_1 and A_2 are 2214.93 and 345.57. The average lifetime τ^* is 4.69 μs (Figure 3f). When excited under a UV light at 352 nm, one broad characteristic band at 448 nm owing to the $^1D_2 \rightarrow {}^3F_4$ transition of the Tm^{3+} ion and the other characteristic bands at 468 nm and 614 nm caused by $^1G_4 \rightarrow {}^3H_6$ and $^1G_4 \rightarrow {}^3F_4$ transitions respectively occur in the emission spectrum of **3** between 405 and 650 nm (Figure 3g). The solid-state sample of **3** emits blue luminescence because of the predominant characteristic band centered at 448 nm. Through monitoring the emission at 448 nm, one tiny peak at 352 nm from the $^3H_6 \rightarrow {}^1D_2$ transition of the Tm^{3+} ion is seen in the excitation spectrum (Figure 3h).[11] The lifetime decay curve of **3** was recorded and is well simulated by the second-order exponential equation (Figure 3i), affording τ_1 of 0.93 μs (31.12%), τ_2 of 8.11 μs (68.88%) A_1 of 1305.95 and A_2 of 330.58. Similarly, τ^* is calculated as 5.87 μs (Table S1a in the supporting information).

Luminescence properties of Ho^{3+}/Tm^{3+} co-doped samples prepared based on 1

It is acknowledged that RE co-doped materials have allured fascinating attention in recent years because of widespread applications in many fields in emission displays, white light-emitting diodes, cathodelumenescence.[18] Their luminescence performances are greatly influenced by energy transfer process between RE species.[19] Thus, we synthesized a series of various molar ratios of Ho^{3+}/Tm^{3+} co-doped POM materials based on **1** by adjusting doping molar ratios of Ho^{3+}/Tm^{3+} (from 0.75:0.25 to 0.25:0.75) to further explore the luminescence properties of RE co-doped POM materials. PXRD and IR spectra are used to testify the whole structures remain unchanged after co-doping RE cations (Figure S5, S6 in the supporting information). Meanwhile, the coexistence of Ho^{3+} and Tm^{3+} in POM architectures is verified by EDS spectra (Figure S7 in the supporting information).

During the course of testing the PL properties of the Ho^{3+}/Tm^{3+} co-doped POM materials, it is essential to know systematically the intramolecular energy transfer (ET) process in the RE co-doped POMs. The intramolecular ET in the RE co-doped POMs can be testified by the following phenomena: (a) The emission band of the donor overlapps with the excitation band of the acceptor, so that the energy can be transferred directly from the donor to the acceptor. (b) With the increasing content of the donor, the fluorescence emission intensity of the acceptor gradually increasing.[20] Herein, under excitation at 352 nm, Tm^{3+} emission bands of Ho^{3+}/Tm^{3+} co-doped materials are located at 448 and 464 nm, which overlap with the Ho^{3+}

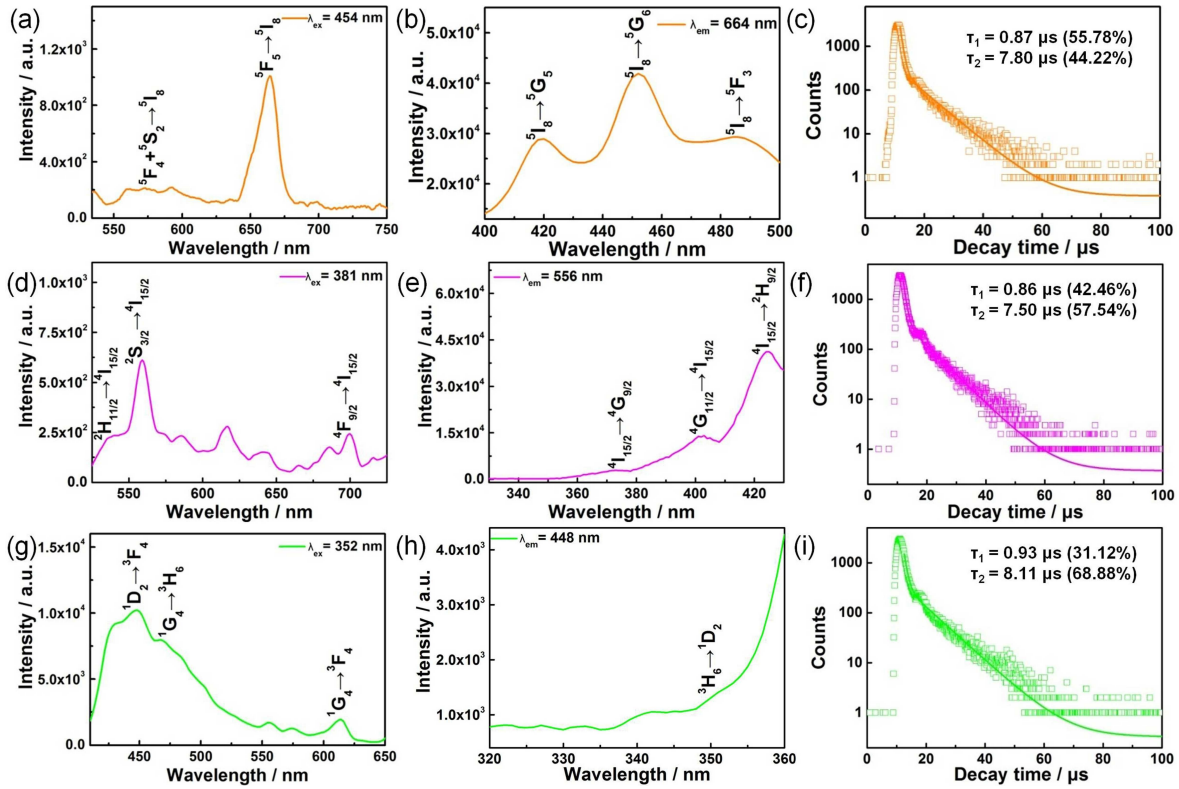

Figure 3. a) PL emission spectrum of **1** upon excitation at 454 nm; b) Excitation spectrum of **1** taken through supervising 664 nm emission; c) Lifetime decay curve of **1** by monitoring 454 nm excitation and 664 nm emission; d) PL emission spectrum of **2** upon excitation at 381 nm; e) Excitation spectrum of **2** taken through supervising 556 nm emission; f) Lifetime decay curve of **2** by monitoring 381 nm excitation and 556 nm emission; g) PL emission spectrum of **3** upon excitation at 352 nm; h) Excitation spectrum of **3** taken through supervising 448 nm emission and i) Lifetime decay curve of **3** by monitoring 352 nm excitation and 448 nm emission.

broad excitation bands centered at 418, 454 and 486 nm taken by monitoring the 664 nm emission, indicating that the Tm^{3+} ions can contribute to enhancing the emission intensity of Ho^{3+} ions in the Ho^{3+}/Tm^{3+} co-doped materials (Figure 4a). When Tm^{3+} ions were excited by an ultraviolet light at 352 nm, electrons located at the $^3H_6$ ground state of Tm^{3+} cations are pumped into the $^1D_2$ excited state and then part of excited electrons undergo non-radiative relaxation return to the $^1G_4$ state because of the spin-orbital coupling interaction, the remaining electrons degenerate to the $^3F_4$ state leading to the emission band of 448 nm. Simultaneously, the radiation transitions of electrons at the $^1G_4$ state result in the $^1G_4 \rightarrow {}^3H_6$ (468 nm) and $^1G_4 \rightarrow {}^3F_4$ (614 nm) emission of Tm^{3+} ions. Because of the matched energy gap between $^1D_2 \rightarrow {}^3F_4$ (448 nm) of Tm^{3+} and $^5I_8 \rightarrow {}^5G_6$ (454 nm) of Ho^{3+} ions, when the excited electrons of Tm^{3+} ions return back to the lower state or the $^3F_4$ ground state from the $^1D_2$ excited state, most of them are trapped by Ho^{3+} ions. And then the trapped electrons relaxed through non-radiative transitions leading to the emission transitions $^5F_4 + {}^5S_2 \rightarrow {}^5I_8$ (575 nm) and $^5F_5 \rightarrow {}^5I_8$ (664 nm) indicating the energy transfer process from Tm^{3+} ions to Ho^{3+} ions (Table S2 in the supporting information, Figure 4b). So, Tm^{3+} ions can be sensitizers to improve the luminescence performance of Ho^{3+} ions. Simultaneously, according to the previous studies, the O→W $^3T_{1u} \rightarrow {}^1A_{1g}$ broad emission band of ST segments at about 470 nm also overlaps with the excitation band of Ho^{3+} centered at 418, 454 and 486 nm, which can indicate that ST segments are beneficial to sensitize the luminescence emission of Ho^{3+} ions by energy transfer from ST segments to Ho^{3+} ions.[21a] When the Ho^{3+}/Tm^{3+} co-doped materials were excited under the excitation band at 352 nm of Tm^{3+} ions, part of energy is absorbed by ST segments and some electrons at the $^1A_{1g}$ ground state of ST segments are pumped to the $^1T_{1u}$ state and then undergo the $^1T_{1u} \rightarrow {}^3T_{1u}$ non-radiative transition because of spin-orbit coupling interaction.[20] Furthermore, when electrons return from the $^3T_{1u}$ triplet state to the $^1A_{1g}$ ground state, some of them are trapped by Ho^{3+} ion, enhancing the emission transitions of $^5F_4 + {}^5S_2 \rightarrow {}^5I_8$ (575 nm) and $^5F_5 \rightarrow {}^5I_8$ (664 nm) of Ho^{3+} ions (Figure 4b). The above results indicate that Tm^{3+} ions and ST segments in the Ho^{3+}/Tm^{3+} co-doped materials can simultaneously promote the emission intensity of Ho^{3+} ions.

Thus, by exciting the Ho^{3+}/Tm^{3+} co-doped samples at the characteristic excitation wavelength of Tm^{3+} ions (352 nm), PL emission spectra of the Ho^{3+}/Tm^{3+} co-doped materials have been recorded (Figure 5a and S8 in the supporting information). In the PL emission spectra, the emission band at around 464 nm and the other characteristic peak at 625 nm are respectively attributed to the $^1D_2 \rightarrow {}^3F_4$ and $^1G_4 \rightarrow {}^3F_4$ transitions of Tm^{3+} ions while the emission bands at around 575, 595 and 648 nm are respectively assigned to $^5F_4 + {}^5S_2 \rightarrow {}^5I_8$ and $^5F_5 \rightarrow {}^5I_8$

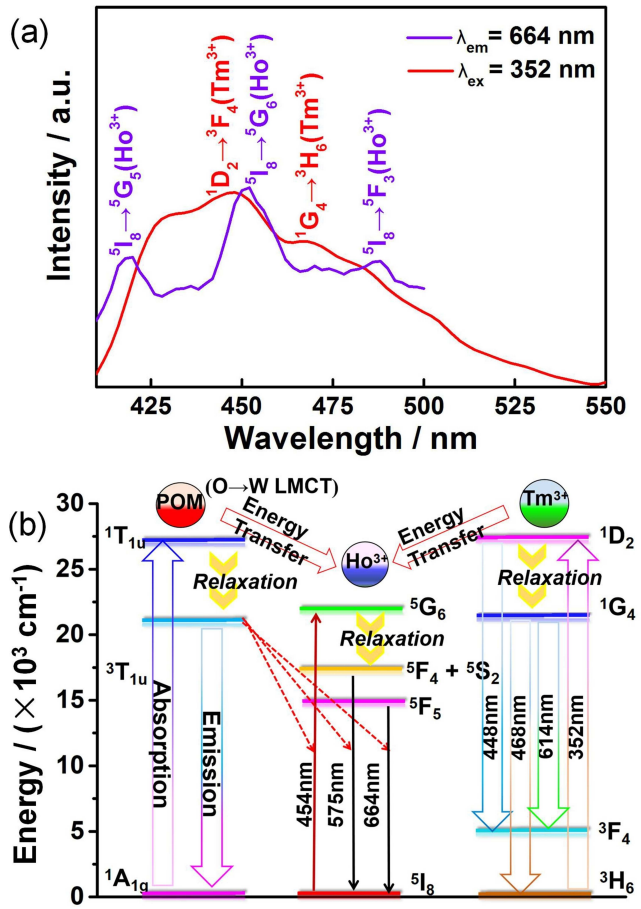

Figure 4. a) Overlapping of the excitation spectrum of Ho^{3+} ions of **1** and emission spectrum of the Tm^{3+} ions of **3** and b) The schematic energy level diagram of Ho^{3+}/Tm^{3+} co-doped samples indicating energy transfer process from Tm^{3+} ions and ST fragments to Ho^{3+} ions.

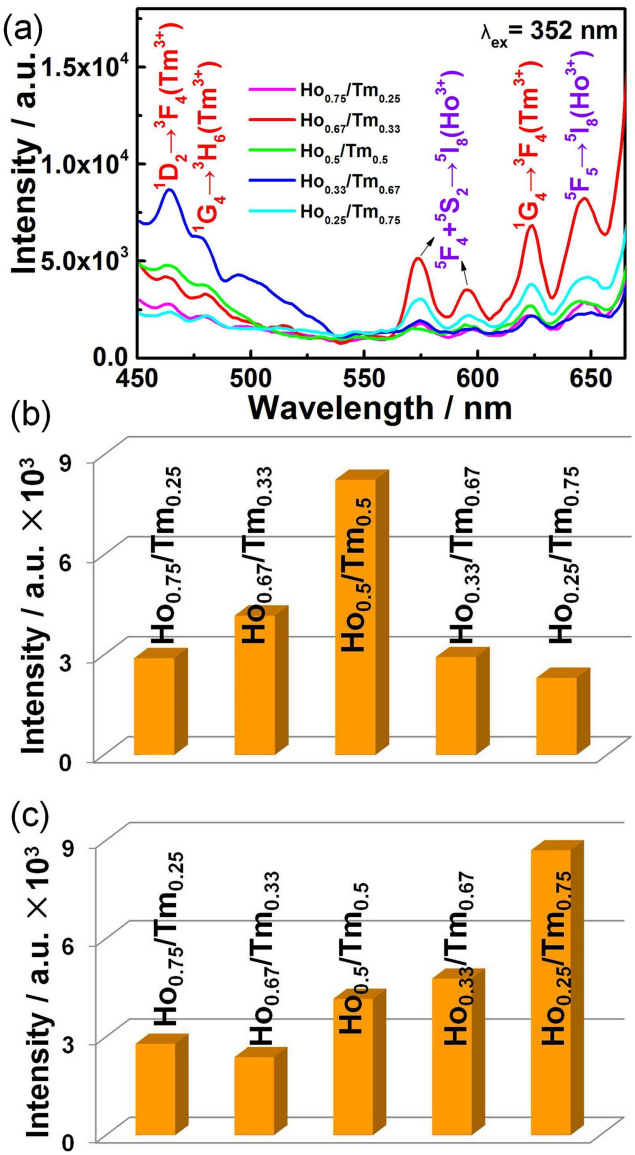

Figure 5. a) Comparison of PL emission spectra between different molar ratio Ho^{3+}/Tm^{3+} co-doped samples under the excitation at 325 nm at room temperature; b) Evolution of the peak emission intensity at 648 nm of various Ho^{3+}/Tm^{3+} co-doped samples and c) Evolution of the peak emission intensity at 464 nm of various Ho^{3+}/Tm^{3+} co-doped samples.

transitions of Ho^{3+} ions. It is obvious that the characteristic emission bands of Tm^{3+} ions are slightly red-shifted and the emission peaks of Ho^{3+} ions are slightly blue-shifted with increasing the doping concentration of Tm^{3+} ions, which can be attributed to the existence of energy transfer from Tm^{3+} to Ho^{3+} ions.[10c] Furthermore, with growing the doping concentration of Tm^{3+} ions, the characteristic emission intensities at 575, 595 and 648 nm of Ho^{3+} ions increase monotonically and reach the maximum at the molar ratio of Ho^{3+}/Tm^{3+} being 0.50:0.50 because of the $Tm^{3+}\rightarrow Ho^{3+}$ energy transfer process.

Afterwards, as further increasing doping ratio of Tm^{3+} ions, the Ho^{3+} emission band decreases promptly (Figure 5b) whereas the Tm^{3+} emission intensity increases instantly because the enhancement of the emission intensity of Tm^{3+} ions surpasses the sensibilization role towards the emission of Ho^{3+} ions. It can be sees that there is no obvious change as for the intensity evolution of Tm^{3+} ions with the elevated concentration of Tm^{3+} in Ho^{3+}/Tm^{3+} co-doped samples at first stage owning to the occurrence of energy transfer from Tm^{3+} ions and ST segments to Ho^{3+} ions whereas the emission intensity of Tm^{3+} ions begins to rise steadily when the molar ratio of Ho^{3+}/Tm^{3+} is higher than 0.5:0.5 because of the dominant emission of Tm^{3+} ions despite the existing energy transfer process from Tm^{3+} and ST segments to Ho^{3+} ions (Figure 5c).

Besides, the decay lifetime curves of the different molar ratio Ho^{3+}/Tm^{3+} co-doped materials are collected and exhibit the similar variation tendency with the emission spectra. When monitoring the emission band at 648 nm of Ho^{3+} cations by using the excitation wavelength of 352 nm, the decay lifetime curves of different molar ratio Ho^{3+}/Tm^{3+} co-doped samples were recorded and were all well fitted with the second-order exponential function (Figure 6a, S9 in the supporting information). The average decay times τ^* responding to various molar ratios were put in Table S1b in the supporting information. As can be seen from Figure 6b, with increasing the Tm^{3+} concentration, the fluorescence lifetime increases monoto-

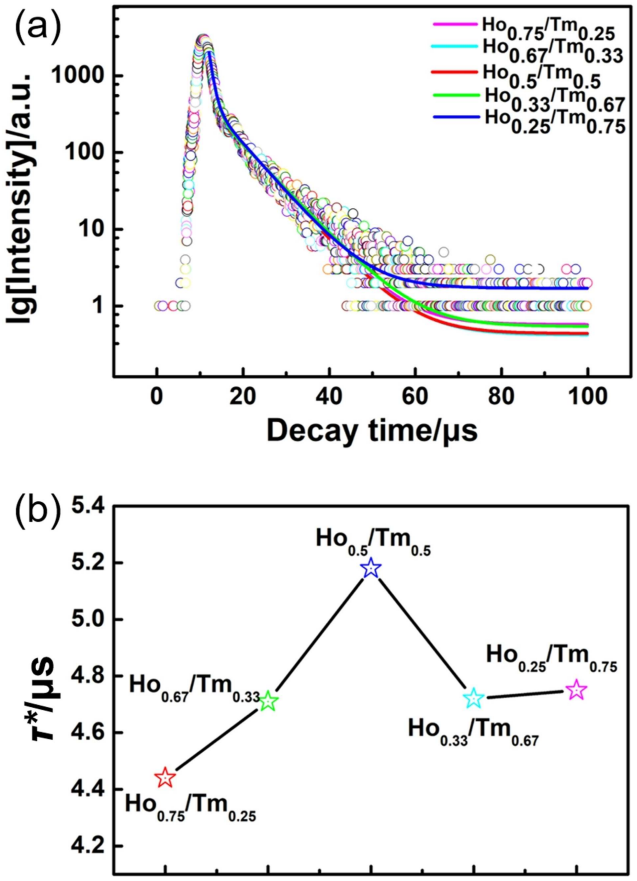

Figure 6. a) The luminescence decay curve of Ho^{3+}/Tm^{3+} co-doped materials monitoring the emission at 648 nm and b) Average decay time evolution of various Ho^{3+}/Tm^{3+} co-doped samples monitoring at 648 nm.

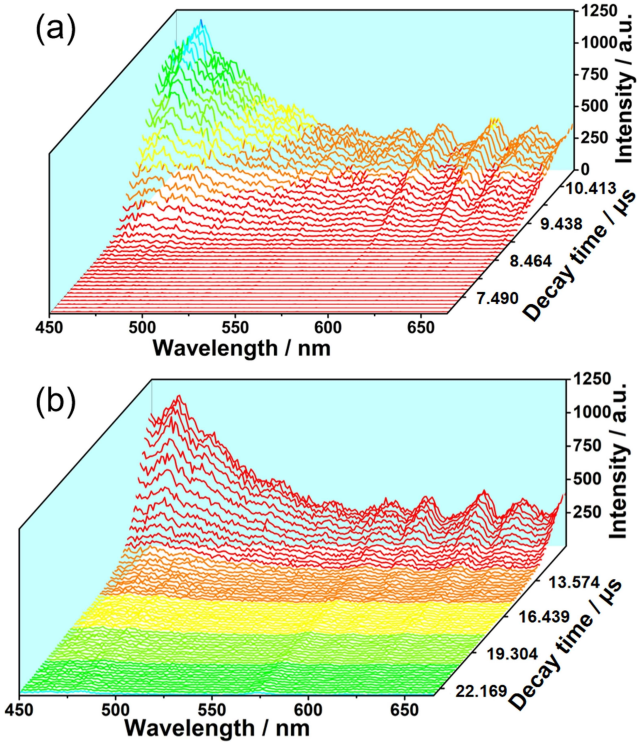

Figure 7. a) TRES of $Ho_{0.5}/Tm_{0.5}$ in the visible region from 7.100–10.900 μs and b) TRES of $Ho_{0.5}/Tm_{0.5}$ in the visible region from 10.900–22.169 μs.

nously till reaches the highest point $\tau^* = 5.18$ μs at **$Ho_{0.5}/Tm_{0.5}$** owning to the occurrence of energy transfer from Tm^{3+} ions and ST segments to Ho^{3+} ions. Then, with further growing Tm^{3+} concentration, the fluorescence lifetime gradually decays to 4.75 μs because the emission contribution of Tm^{3+} ions becomes dominant and exceeds the sensibilization function of Tm^{3+} ions and ST segments towards Ho^{3+} ions.

With the purpose of demonstrating energy transfer process from Tm^{3+} ions and ST segments to Ho^{3+} ions in the Ho^{3+}/Tm^{3+} co-doped materials, the TRES measurement of the optimum **$Ho_{0.5}/Tm_{0.5}$** as a representative was performed under the excitation of 352 nm and in the emission range of 450–665 nm (Figure 7). In the time period of 7.100–10.900 μs, the emission peaks of Tm^{3+} and Ho^{3+} ions simultaneously appear in the emission spectrum and their emission intensities reach the maximum at 10.900 μs (Figure 7a). Afterwards, the emission intensities of Tm^{3+} and Ho^{3+} ions reduce with the prolonging time (10.900–22.169 μs). It should be worth noting that the decay rate of the emission intensity of Ho^{3+} ions is slower than that of Tm^{3+} ions upon increasing time (Figure 7b), because the decay intensity of the emission peaks of Ho^{3+} ions can be to some extent inhibited by the sensitization of Tm^{3+} ions and ST segments toward the emission of Ho^{3+} ions, which manifests the existence of energy transfer from Tm^{3+} ions and ST segments to Ho^{3+} ions. Furthermore, in the beginning of decay (10.900–12.237 μs), the emission intensity of the characteristic band of Tm^{3+} ions decreases rapidly while the emission peak of Ho^{3+} ions remains almost uncharged (Figure 8a), which also vividly consolidates the energy transfer process from Tm^{3+} ions and ST segments to Ho^{3+} ions. What's more, the energy transfer between Tm^{3+} and Ho^{3+} ions are very obviously observed when the decay time is in the range of 10.900–11.644 μs. It can be seen from Figure 8b that the emission intensity of Tm^{3+} ions at 464 nm sharply decreases with the emission intensity of Ho^{3+} ions at 648 nm attenuating slowly, which further testifies that the sensitization of Tm^{3+} ions to Ho^{3+} ions.

In addition, the fluorescence emitting colors of co-doped samples can be represented in CIE 1931 chromaticity diagram. It can be obviously seen from Figure 9 that the color coordinates of **1** and **3** are respectively located in the red and blue region. As for the family of Ho^{3+}/Tm^{3+} co-doped materials upon excitation at 352 nm, **$Ho_{0.75}/Tm_{0.25}$** emits purple light. With increasing the concentration of Tm^{3+} ions in Ho^{3+}/Tm^{3+} co-doped materials (**$Ho_{0.67}/Tm_{0.33}$** and **$Ho_{0.5}/Tm_{0.5}$**), no obvious color change is observed owing to the existence of energy transfer from Tm^{3+} ions and ST segments to Ho^{3+} ions. However, the fluorescence color changes obviously from purple to blue with further increasing the amount of Tm^{3+} ions (**$Ho_{0.33}/Tm_{0.67}$** and **$Ho_{0.25}/Tm_{0.75}$**) due to the dominant emission of Tm^{3+} ions in spite of the existence of energy transfer from Tm^{3+} and ST segments to Ho^{3+} ions. Based on the above analysis, the content of Tm^{3+} ion makes a significant influence on the

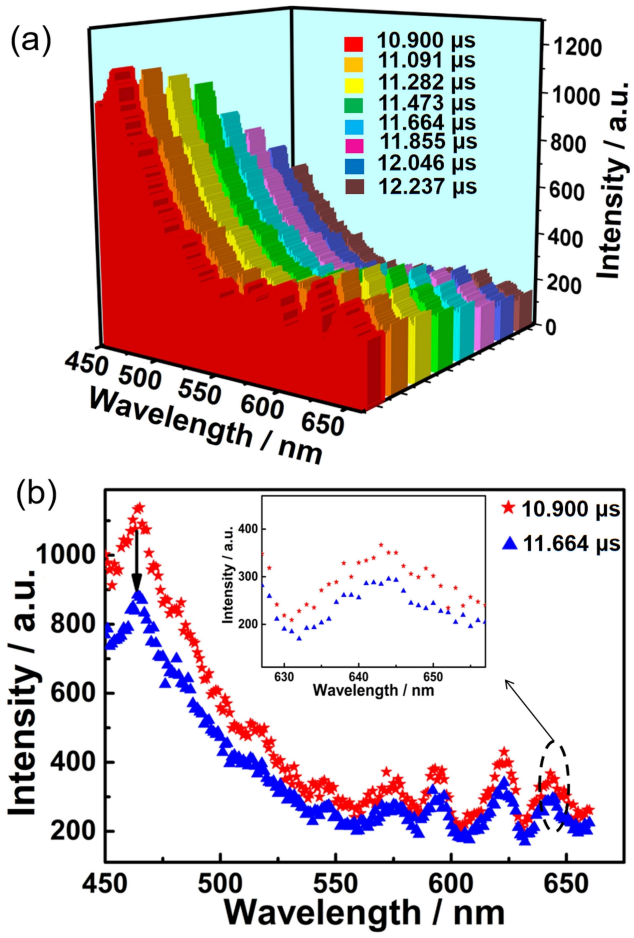

Figure 8. a) TRES of $Ho_{0.5}/Tm_{0.5}$ in the visible region from 10.900 to 12.237 μs and b) TRES of $Ho_{0.5}/Tm_{0.5}$ in the visible region at 10.900 and 11.664 μs.

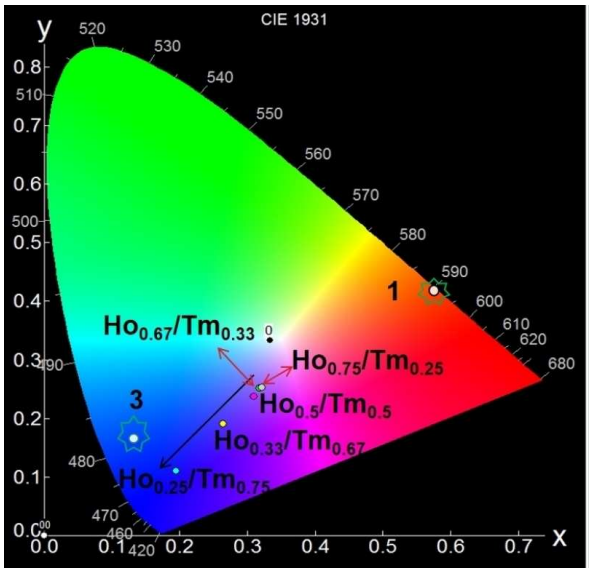

Figure 9. CIE 1931 diagram of **1**, **3** and various molar ratio Ho^{3+}/Tm^{3+} co-doped materials.

emitting color and suggests a general route of various mixed RE co-doped materials to tune luminescence emitting color.

Conclusion

In conclusion, a series of tetravacant penta-RE incorporated Dawson STs $[H_2N(CH_3)_2]_{10}H_3[SeO_4RE_5(H_2O)_7(Se_2W_{14}O_{52})_2]\cdot 40H_2O$ [RE = Ho^{3+} (1), Er^{3+} (2), Tm^{3+} (3), Tb (4)] were synthesized in the conventional aqueous solution. It is clearly seen that the $[SeO_4RE_5(H_2O)_7]^{11+}$ segment is sandwiched by two equal tetravacant $[Se_2W_{14}O_{52}]^{12-}$ building blocks forming the dimeric $[SeO_4RE_5(H_2O)_7(Se_2W_{14}O_{52})_2]^{13-}$ polyanion. Strikingly, the four-coordinate {SeO_4} bridging group is observed rarely in the field of POM chemistry. Based on the fluorescence measurements, the energy level $^1D_2 \rightarrow {}^3F_4$ (448 nm) of Tm^{3+} ions matches well with $^5I_8 \rightarrow {}^5G_6$ (454 nm) of Ho^{3+} ions supporting the exploration for energy transfer. Under this guidance, we synthesized a series of Ho^{3+}/Tm^{3+} co-doped solid samples via precise control of different dopant concentration combinations of Ho^{3+} and Tm^{3+} ions and further set out to explore energy transfer by exciting the co-doped samples at the characteristic excitation band of Tm^{3+} ions at 352 nm. According to the systematic studies on fluorescence intensity and lifetime of various molar ratio Ho^{3+}/Tm^{3+} co-doped samples, sensitization of Tm^{3+} ions enhances the emission intensity of Ho^{3+} ions and prolongs the lifetime of Ho^{3+} ions at the same time, reaching the maximum at the molar ratio of Ho^{3+}/Tm^{3+} being 0.5:0.5. Moreover, CIE diagrams of Ho^{3+}/Tm^{3+} co-doped samples show changeable emission colors from purple to blue light accompanying the consecutive amount of Tm^{3+} ions under f-f excitation of RE ions. The above results indicate that the Tm^{3+} ions are able to sensitize the Ho^{3+} ions to improve the emission intensity in the visible region; meanwhile, the Ho^{3+}/Tm^{3+} molar variation in co-doped samples can adjust the fluorescence color. This work not only provides a simple approach for preparing new hetero-RE co-doped POM materials but also contributes to broaden the potential applications of RE–POM materials in the field of lighting materials and W-LEDs. In our following work, we will concentrate on the preparation of novel multi-nuclear-RE substituted POMs and studies on multicolor-tuning and white-light emission of POM-based materials by introducing various RE ions in doped systems.

Experimental Section

Materials and methods

All chemical reagents are commercially purchased and used without further purification. The Perkin-Elmer 2400-II CHNS/O analyser was used to perform C, H and N elemental analyses. IR spectra were obtained from solid samples palletized with KBr on a Bruker Vertex 70 IR spectrometer ranging from 4000–500 cm^{-1}. PXRD patterns were conducted by using a Bruker AXS D8 Advance diffractometer with Cu Kα radiation (λ = 1.54056 Å) at 293 K. TG analyses were recorded on a Mettler-Toledo TGA/SDTA 851^e instrument under a flowing N_2 atmosphere with a heating rate of 10 °C min^{-1} from 25

Table 1. X-ray diffraction crystallographic data and structure refinements for **1**–**4**.

	1	2	3	4
Empirical formula	$C_{20}H_{177}Ho_5N_{10}O_{155}Se_5W_{28}$	$C_{20}H_{177}Er_5N_{10}O_{155}Se_5W_{28}$	$C_{20}H_{177}Tm_5N_{10}O_{155}Se_5W_{28}$	$C_{20}H_{177}Tb_5N_{10}O_{155}Se_5W_{28}$
Formula weight	9405.97	9417.62	9425.97	9379.95
Crystal system	Monoclinic	Monoclinic	Monoclinic	Monoclinic
Space group	*C*2/m	*C*2/m	*C*2/m	*C*2/m
a, Å	23.769(1)	23.657(2)	23.703(1)	23.827(2)
b, Å	25.869(0)	25.688(2)	26.270(4)	25.905(2)
c, Å	18.053(5)	17.922(2)	18.000(6)	18.060(0)
α, deg	90	90	90	90
β, deg	126.0010(10)	126.353(0)	126.300(0)	126.032(0)
γ, deg	90	90	90	90
V, Å^{-3}	8980.6(9)	8771.6(13)	9033.5(11)	9014.8(15)
Z	2	2	2	2
μ, mm^{-1}	21.144	21.784	21.286	20.831
F(000)	8368	8378	8388	8356
T, K	296(2)	296(2)	296(2)	296(2)
Limiting indices	$-28 \le h \le 21$ $-26 \le k \le 30$ $-21 \le l \le 21$	$-13 \le h \le 28$ $-29 \le k \le 30$ $-21 \le l \le 21$	$-25 \le h \le 28$ $-31 \le k \le 30$ $-20 \le l \le 21$	$-28 \le h \le 27$ $-30 \le k \le 28$ $-21 \le l \le 21$
Reflections collected/unique	22882/7952	22171/7716	22737/7941	22263/7892
R_{int}	0.0527	0.0476	0.0498	0.0616
Data/restrains/parameters	7952/13/419	7716/7/420	7941/19/411	7892/26/416
GOF on F^2	1.035	1.053	1.022	1.004
R_1, wR_2 ($I > 2\sigma(I)$)	0.0449, 0.1083	0.0399, 0.0983	0.0438, 0.1108	0.0476, 0.1116
R_1, wR_2 (all data)	0.0716, 0.1175	0.0569, 0.1042	0.0680, 0.1205	0.0765, 0.1218

to 800 °C. PL spectra were tested on an FLS 980 Edinburgh Analytical Instrument with a 450 W xenon lamp. PL decay lifetime and time-resolved emission spectra were recorded by an excitation source of μF900H high-energy microsecond flash lamp.

Synthesis of $[H_2N(CH_3)_2]_{10}H_3[SeO_4Ho_5(H_2O)_7(Se_2W_{14}O_{52})_2]\cdot 40H_2O$ (1)

Na_2SeO_3 (0.400 g, 2.324 mmol), $Na_2WO_4\cdot 2H_2O$ (2.500 g, 7.579 mmol), 2,6-pyridinedicarboxylic acid (0.102 g, 0.598 mmol), dimethylamine hydrochloride (1.000 g, 12.264 mmol) were successively dissolved in 15 mL water with constantly stirring. The pH value of the settled solution was adjusted to 5.55 by 6 mol·L^{-1} HCl. Then $Ho(NO_3)_3\cdot 6H_2O$ (0.400 g, 0.871 mmol) was added and the pH value was kept at 5.51 by adding 4 mol·L^{-1} NaOH. The resulting solution was kept in a 90 °C water bath for 1 h, cooled and filtered. Slow evaporation of the filtrate at ambient temperature for approximately 4 days, light yellow block crystals of **1** were obtained. Yield: 0.68 g (*ca.* 41.50% based on $Ho(NO_3)_3\cdot 6H_2O$). Anal. calcd. (found%) for $C_{20}H_{177}Ho_5N_{10}O_{155}Se_5W_{28}$ (**1**): H 1.90 (2.12), C 2.55 (2.60), N 1.49 (1.21), Se 4.20 (4.08), Ho 8.77 (8.58), W 54.73 (54.53).

Synthesis of $[H_2N(CH_3)_2]_{10}H_3[SeO_4Er_5(H_2O)_7(Se_2W_{14}O_{52})_2]\cdot 40H_2O$ (2)

The synthesis of **2** is similar to **1** except that $Er(NO_3)_3\cdot 6H_2O$ (0.400 g, 0.867 mmol) replaces $Ho(NO_3)_3\cdot 6H_2O$. Pink block crystals of **2** were obtained. Yield: 0.74 g (*ca.* 45.32% based on $Er(NO_3)_3\cdot 6H_2O$). Anal. calcd. (found%) for $C_{20}H_{177}Er_5N_{10}O_{155}Se_5W_{28}$ (**2**): H 1.89 (2.09), C 2.55 (2.64), N 1.49 (1.20), Se 4.19 (4.05), Er 8.88 (8.69), W 54.66 (54.47).

Synthesis of $[H_2N(CH_3)_2]_{10}H_3[SeO_4Tm_5(H_2O)_7(Se_2W_{14}O_{52})_2]\cdot 40H_2O$ (3)

The synthesis of **3** is similar to **1** except that $Tm(NO_3)_3\cdot 6H_2O$ (0.400 g, 0.864 mmol) replaces $Ho(NO_3)_3\cdot 6H_2O$. Colorless block crystals of **3** were obtained. Yield: 0.70 g (*ca.* 42.94% based on Tm $(NO_3)_3\cdot 6H_2O$). Anal. calcd. (found%) for $C_{20}H_{177}Tm_5N_{10}O_{155}Se_5W_{28}$ (**3**): H 1.88 (2.03), C 2.55 (2.67), N 1.49 (1.21), Se 4.19 (4.02), Tm 8.96 (8.75), W 54.61 (54.41).

Synthesis of $[H_2N(CH_3)_2]_{10}H_3[SeO_4Tb_5(H_2O)_7(Se_2W_{14}O_{52})_2]\cdot 40H_2O$ (4)

The synthesis of **4** is similar to **1** except that $Tb(NO_3)_3\cdot 6H_2O$ (0.400 g, 0.883 mmol) replaces $Ho(NO_3)_3\cdot 6H_2O$. Colorless block crystals of **4** were obtained. Yield: 0.67 g (*ca.* 40.43% based on Tb $(NO_3)_3\cdot 6H_2O$). Anal. calcd. (found%) for $C_{20}H_{177}Tb_5N_{10}O_{155}Se_5W_{28}$ (**4**): H 1.90 (2.08), C 2.56 (2.71), N 1.49 (1.31), Se 4.21 (3.99), Tb 8.48 (8.57), W 54.90 (54.62).

Synthesis of Ho^{3+}/Tm^{3+} co-doped samples

The synthetic process of Ho^{3+}/Tm^{3+} co-doped samples are exactly same as **1** except that a mixture of $Ho(NO_3)_3\cdot 6H_2O/Tm(NO_3)_3\cdot 6H_2O$ is in place of $Ho(NO_3)_3\cdot 6H_2O$. At the same time, the mixture with different molar ratios but the total mass of $Tm(NO_3)_3\cdot 6H_2O$ and Ho $(NO_3)_3\cdot 6H_2O$ is remain unchanged. The different molar ratios of Ho $(NO_3)_3\cdot 6H_2O/Tm(NO_3)_3\cdot 6H_2O$ are set as 0.75:0.25, 0.67:0.33, 0.5:0.5, 0.33:0.67, 0.25:0.75. For simplicity, the resulting Ho^{3+}/Tm^{3+} co-doped samples are called as **$Ho_{0.75}/Tm_{0.25}$**, **$Ho_{0.67}/Tm_{0.33}$**, **$Ho_{0.5}/Tm_{0.5}$**, **$Ho_{0.33}/Tm_{0.67}$**, **$Ho_{0.25}/Tm_{0.75}$**, respectively. Light yellow crystals of a series of Ho^{3+}/Tm^{3+} co-doped samples were obtained. Yield: **$Ho_{0.75}/Tm_{0.25}$** 0.74 g, **$Ho_{0.67}/Tm_{0.33}$** 0.69 g, **$Ho_{0.5}/Tm_{0.5}$** 0.71 g, **$Ho_{0.33}/Tm_{0.67}$** 0.73 g, **$Ho_{0.25}/Tm_{0.75}$** 0.68 g.

X-ray crystallography

Pure perfect crystals of **1**–**4** were picked up from mother solution and fiber glasses were used for storing good-quality crystals to collect intensity data. Diffraction intensity data for **1**–**4** were measured on a Bruker CCD Apex II diffractometer with Mo Kα monochromated radiation ($\lambda = 0.71073$ Å) at 296 K. The SHELXTL-97 program was applied for analyzing the structures and locate the heavy atoms by direct methods. The remaining atoms were found from successive full-matrix least-squares refinements on F^2 and Fourier syntheses. No hydrogen atoms associated with water

molecules were located from the difference Fourier map. All non-hydrogen atoms were refined anisotropically except for some water molecules. However, there exist very large solvent accessible voids in their check cif reports, suggesting that some lattice water molecules or cations should exist in the structures that cannot be found from the weak residual electron peaks. These water molecules or cations are highly disordered, and attempts to locate and refine them were unsuccessful. On the basis of elemental analyses and TG analyses, 28 lattice water molecules and 6 $[H_2N(CH_3)_2]^+$ cations were directly added to the molecular formula of **1**–**4**. Crystallographic data and structural refinements for **1**–**4** are summarized in Table 1. CIF files for **1**–**4** reported in this paper have been deposited in the Cambridge Crystallographic Data Centre with CCDC 1917296–1917298 and 1982250. These data can be obtained free of charge from the Cambridge Crystallographic Data Centre via www.ccdc.cam.ac.uk/data_request/cif, or by emailing data_request@ccdc.cam.ac.uk, or by contacting The Cambridge Crystallographic Data Centre, 12, Union Road, Cambridge CB2 1EZ, UK; fax: +44 1223 336033.

Acknowledgements

This work was supported by the National Natural Science Foundation of China (21671054, 21571048, 21771052, 21871077), the Program for Innovation Teams in Science and Technology in Universities of Henan Province (20IRTSTHN004), the Program of First-Class Discipline Cultivation Project of Henan University (2019YLZDYJ02), the Postgraduate Education Innovation and Quality Improvement Plan of Henan University (SYL18060130) and the 2018 Students Innovative Pilot Plan of Henan University (201810475014).

Keywords: polyoxometalate · selenotungstate · lanthanide · sandwich complexes · luminescent properties

[1] a) E. Coronado, C. J. Gómez-García, *Chem. Rev.* **1998**, *98*, 273–296; b) A. Saad, O. Oms, A. Dolbecq, C. Menet, R. Dessapt, H. Serier-Brault, E. Allard, K. Baczko, P. Mialane, *Chem. Commun.* **2015**, *51*, 16088–16091; c) A. González, N. Gálvez, M. Clemente-León, J. M. Dominguez-Vera, *Chem. Commun.* **2015**, *51*, 10119–10122; d) X. Ma, W. Yang, L. J. Chen, J. W. Zhao, *CrystEngComm* **2015**, *17*, 8175–8197; e) J. Cai, X.-Y. Zheng, J. Xie, Z.-H. Yan, X.-J. Kong, Y.-P. Ren, L.-S. Long, L.-S. Zheng, *Inorg. Chem.* **2017**, *56*, 8439–8445; f) J.-C. Liu, Q. Han, L.-J. Chen, J.-W. Zhao, C. Streb, Y.-F. Song, *Angew. Chem. Int. Ed.* **2018**, *57*, 8416–8420; g) S. J. Folkman, J. Soriano-Lopez, J. R. Galán-Mascarós, R. G. Finke, *J. Am. Chem. Soc.* **2018**, *140*, 12040–12055.

[2] a) T. M. Anderson, R. Cao, E. Slonkina, B. Hedman, K. O. Hodgson, K. I. Hardcastle, W. A. Neiwert, S. X. Wu, M. L. Kirk, S. Knottenbelt, E. C. Depperman, B. Keita, L. Nadjo, D. G. Musaev, K. Morokuma, C. L. Hill, *J. Am. Chem. Soc.* **2005**, *127*, 11948–11949; b) L.-H. Bi, G.-F. Hou, B. Li, L.-X. Wu, U. Kortz, *Dalton Trans.* **2009**, 6345–6353; c) W.-W. Ju, H.-T. Zhang, X. Xu, Y. Zhang, Y. Xu, *Inorg. Chem.* **2014**, *53*, 3269–3271; d) Y. M. Li, H. L. Li, J. Jiang, L. J. Chen, J. W. Zhao, *Inorg. Chem.* **2019**, *58*, 3479–3491; e) Z. Li, X.-X. Li, B. Li, T. Yang, Z.-W. Cai, S.-T. Zheng, *Angew. Chem. Int. Ed.* **2017**, *56*, 2664–2669; f) L. Jin, X.-X. Li, Y.-J. Qi, P.-P. Niu, S.-T. Zheng, *Angew. Chem. Int. Ed.* **2016**, *55*, 13793–13797; *Angew. Chem.* **2016**, *128*, 13997–14001.

[3] a) J. M. Cameron, J. Gao, D.-L. Long, L. Cronin, *Inorg. Chem. Front.* **2014**, *1*, 178–185; b) W.-C. Chen, C. Qin, Y.-G. Li, H.-Y. Zang, K.-Z. Shao, Z.-M. Su, E.-B. Wang, *Chem-Asian J.* **2015**, *10*, 1184–1191; c) L. Yang, L. Li, J. P. Guo, Q. S. Liu, P. T. Ma, J. Y. Niu, J. P. Wang, *Chem. Asian J.* **2017**, *12*, 2441–2446; d) T.-T. Yan, Z.-X. Xuan, S. Wang, X. Zhang, F. Luo, *Inorg. Chem. Commun.* **2019**, *105*, 147–150.

[4] a) W.-C. Chen, C. Qin, X.-L. Wang, C.-X. Wu, Y.-G. Li, H.-Y. Zang, K.-Z. Shao, Z.-M. Su, E.-B. Wang, *CrystEngComm* **2016**, *18*, 2820–2824; b) Q. Han, Y. Wen, J.-C. Liu, W. Zhang, L.-J. Chen, J.-W. Zhao, *Inorg. Chem.* **2017**, *56*, 13228–13240.

[5] a) J. P. Wang, P. T. Ma, J. Y. Niu, *Inorg. Chem. Commun.* **2006**, *9*, 1049–1052; b) J. Gao, J. Yan, S. Beeg, D.-L. Long, L. Cronin, *J. Am. Chem. Soc.* **2013**, *135*, 1796–1805; c) W.-C. Chen, C. Qin, X.-L. Wang, Y.-G. Li, H.-Y. Zang, Y.-Q. Jiao, P. Huang, K.-Z. Shao, Z.-M. Su, E.-B. Wang, *Chem. Commun.* **2014**, *50*, 13265–13267; d) W. C. Chen, C. Qin, X.-L. Wang, K.-Z. Shao, Z.-M. Su, E.-B. Wang, *Cryst. Growth Des.* **2016**, *16*, 2481–2486; e) W.-C. Chen, H.-L. Li, X.-L. Wang, K.-Z. Shao, Z.-M. Su, E.-B. Wang, *Chem. Eur. J.* **2013**, *19*, 11007–11015; f) J. M. Cameron, J. Gao, L. Vilà-Nadal, D.-L. Long, L. Cronin, *Chem. Commun.* **2014**, *50*, 2155–2157; g) J. Yan, J. Gao, D.-L Long, H. N. Miras, L. Cronin, *J. Am. Chem. Soc.* **2010**, *132*, 11410–11411; h) M. A. Moussawi, S. Floquet, P. A. Abramov, C. Vicent, M. Haouas, E. Cadot, *Inorg. Chem.* **2018**, *57*, 56–63; i) W.-C. Chen, S.-T. Wu, X.-L. Wang, C. Qin, Z.-M. Su, K.-Z. Shao, E.-B. Wang, *Dalton Trans.* **2018**, *47*, 1393–1397.

[6] a) S. X. Shang, Z. G. Lin, A. X. Yin, S. Yang, Y. N. Chi, Y. Wang, J. Dong, B. Liu, N. Zhen, C. L. Hill, C. W. Hu, *Inorg. Chem.* **2018**, *57*, 8831–8840; b) Y.-J. Wang, S.-Y. Wu, Y.-Q. Sun, X.-X. Li, S.-T. Zheng, *Chem. Commun.* **2019**, *55*, 2857–2860; c) W.-C. Chen, L.-K. Yan, C.-X. Wu, X.-L. Wang, K.-Z. Shao, Z.-M. Su, E.-B. Wang, *Cryst. Growth Des.* **2014**, *14*, 5099–5110; d) H.-L. Li, C. Lian, L.-J. Chen, J.-W. Zhao, G.-Y. Yang, *Inorg. Chem.* **2019**, *58*, 8442–8450.

[7] J.-W. Zhao, Y.-Z. Li, L.-J. Chen, G.-Y. Yang, *Chem. Commun.* **2016**, *52*, 4418–4445.

[8] a) Q.-Y. Yang, M. Pan, S.-C. Wei, K. Li, B.-B. Du, C.-Y. Su, *Inorg. Chem.* **2015**, *54*, 5707–5716; b) G. D. Fura, Y. Long, J. Yan, W. Chen, C.-G. Lin, Y.-F. Song, *Acta Crystallogr.* **2018**, *C74*, 1260–1266.

[9] a) J. H. Oh, J. R. Oh, H. K. Park, Y.-G. Sung, Y. R. Do, *Opt. Express* **2011**, *19*, A270–A279; b) X. Min, Z. H. Huang, M. H. Fang, Y.-G. Liu, C. Tang, X. W. Wu, *Inorg. Chem.* **2014**, *53*, 6060–6065.

[10] a) H. C. Wu, B. Yan, H. F. Li, V. Singh, P. T. Ma, J. Y. Niu, J. P. Wang, *Inorg. Chem.* **2018**, *57*, 7665–7675; b) J.-L. Liu, M.-T. Jin, L.-J. Chen, J.-W. Zhao, *Inorg. Chem.* **2018**, *57*, 12509–12520; c) R. Praveena, V. S. Sameera, P. Babu, C. Basavapoornima, C. K. Jayasankar, *Opt. Mater.* **2017**, *72*, 666–672.

[11] H.-L. Li, Y.-J. Liu, J.-L. Liu, L.-J. Chen, J.-W. Zhao, G.-Y. Yang, *Chem. Eur. J.* **2017**, *23*, 2673–2689.

[12] P. J. Gong, J. J. Pang, C. P. Zhai, J. W. Zhao, *Solid State Sci.* **2018**, *78*, 7–15.

[13] a) Q. Liu, W. Feng, F. Y. Li, *Coord. Chem. Rev.* **2014**, *273*, 100–110; b) R. Wang, X. M. Li, L. Zhou, F. Zhang, *Angew. Chem. Int. Ed.* **2014**, *53*, 12086–12090; *Angew. Chem.* **2014**, *126*, 12282–12286; c) A. Stepuk, G. Casola, C. M. Schumacher, K. W. Krämer, W. J. Stark, *Chem. Mater.* **2014**, *26*, 2015–2020; d) L. Marciniak, K. Prorok, A. Bednarkiewicz, *J. Mater. Chem. C* **2017**, *5*, 7890–7897; e) B. P. Kore, A. Kumar, A. Pandey, R. E. Kroon, J. J. Terblans, S. J. Dhoble, H. C. Swart, *Inorg. Chem.* **2017**, *56*, 4996–5005; f) G. Galleani, S. H. Santagneli, Y. Ledemi, Y. Messaddeq, O. Janka, R. Pöttgen, H. Eckert, *J. Phys. Chem. C* **2018**, *122*, 2275–2284.

[14] a) G. T. Xiang, Y. Ma, W. Liu, S. Jiang, X. B. Luo, L. Li, X. J. Zhou, Z. W. Gu, J. P. Wang, Y. S. Luo, J. H. Zhang, *Inorg. Chem.* **2017**, *56*, 9194–9199; b) H. Jia, Z. L. Liu, L. M. Liao, Y. H. Gu, C. L. Ding, J. G. Zhao, W. Y. Zhang, X. K. Hu, X. Feng, Z. Chen, X. F. Liu, J. R. Qiu, *J. Phys. Chem. C* **2018**, *122*, 9606–9610; c) Y. H. Chen, L. H. Sun, S. Z. Chang, L. J. Chen, J. W. Zhao, *Inorg. Chem.* **2018**, *57*, 15079–15092; d) J. Jiang, J. R. Duan, J. C. Liu, L. J. Chen, J. W. Zhao, *Cryst. Growth Des.* **2020**, *20*, 362–369.

[15] a) C.-H. Huang, T.-M. Chen, W.-R. Liu, Y.-C. Chiu, Y.-T. Yeh, S.-M. Jang, *ACS Appl. Mater. Interfaces* **2010**, *2* 259–264; b) C.-H. Huang, T.-M. Chen, *J. Phys. Chem. C* **2011**, *115*, 2349–2355; c) G. G. Li, Y. Zhang, D. L. Geng, M. M. Shang, C. Peng, Z. Y. Cheng, J. Lin, *ACS Appl. Mater. Interfaces* **2012**, *4*, 296–305.

[16] R. Martín-Rodríguez, S. Fischer, A. Ivaturi, B. Froehlich, K. W. Krämer, J. C. Goldschmidt, B. S. Richards, A. Meijerink, *Chem. Mater.* **2013**, *25*, 1912–1921.

[17] a) D. He, C. F. Guo, S. S. Zhou, L. L. Zhang, Z. Yang, C. K. Duan, M. Yin, *CrystEngComm* **2015**, *17*, 7745–7753; b) F. Wang, X. G. Liu, *J. Am. Chem. Soc.* **2008**, *130*, 5642–5643; c) J. Jiang, Y. H. Chen, L. L. Liu, L. J. Chen, J. W. Zhao, *Inorg. Chem.* **2019**, *58*, 15853–15863.

[18] a) J. H. Hao, S. A. Studenikin, M. Cocivera, *J. Lumin.* **2001**, *93*, 313–319; b) P. Du, L. L. Wang, J. S. Yu, *J. Alloys Compd.* **2016**, *673*, 426–432; c) Y. L. Zhang, X. H. Liu, Y. B. Lang, Z. Yuan, D. Zhao, G. S. Qin, W. P. Qin, *J. Mater. Chem. C* **2015**, *3*, 2045–2053; d) J. Tan, S. He, S. Yan, Y. Li, H. Li, H. Zhang, L. Zhao, L. Li, *Protoplasma* **2014**, *251*, 1213–1221.

[19] a) M. M. Shang, D. L. Geng, X. J. Kang, D. M. Yang, Y. Zhang, J. Lin, *Inorg. Chem.* **2012**, *51*, 11106–11116; b) T. Wei, Y. Tian, C. Tian, M. Z. Cai, X. F. Jing, B. P. Li, R. Chen, J. J. Zhang, S. Q. Xu, *J. Phys. Chem. A* **2015**, *119*, 6823–6830; c) W. M. Gao, T. Yu, L. X. Wu, L. H. Bi, *Chem. Commun.* **2016**, *52*, 10403–10406; d) Q. Y. Tang, H. P. Xia, S. N. He, Q. G. Sheng, B. J. Chen, *Opt. Laser Technol.* **2017**, *96*, 70–75; e) L. Li, M. Hou, L. Cao, Y. Xia, Z. Shen, Z. Hu, *Environ. Exp. Bot.* **2018**, *155*, 313–320.

[20] X. Xu, H. L. Li, S. S. Xie, L. Mei, R. R. Meng, L. J. Chen, J. W. Zhao, *Inorg. Chem.* **2020**, *59*, 648–660.

[21] a) Y. Zhang, Y. M. Li, J. J. Pang, Y. F. Liu, P. Li, L. J. Chen, J. W. Zhao, *Inorg. Chem.* **2019**, *58*, 7078–7090; b) T. Yamase, *Chem. Rev.* **1998**, *98*, 307–326.

Manuscript received: January 30, 2020
Revised manuscript received: February 9, 2020
Accepted manuscript online: February 10, 2020
Version of record online: March 9, 2020